Journal of The Electrochemical Society, 2020 **167** 090542

Fingerprinting Redox Heterogeneity in Electrodes during Extreme Fast Charging

Aashutosh Mistry,[1,*,a] Francois L. E. Usseglio-Viretta,[2] Andrew Colclasure,[2] Kandler Smith,[2,*] and Partha P. Mukherjee[1,*,z]

[1]*School of Mechanical Engineering, Purdue University, West Lafayette, Indiana 47907, United States of America*
[2]*Transportation and Hydrogen Systems Center, National Renewable Energy Laboratory, Golden, Colorado 80401, United States of America*

Conventionally, battery electrodes are rationalized as homogeneous reactors. It proves to be an erroneous interpretation for fast transients, where mass transport limitations amplify underlying heterogeneities. Given the lack of observability of associated fast spatiotemporal dynamics, redox activity in inhomogeneous electrodes is superficially explored. We resort to a physics-based description to examine the extreme fast charging of lithium-ion battery electrodes. Representative inhomogeneity information is extracted from electrode tomograms. We discover such electrodes to undergo preferential intercalation, localized lithium plating and nonuniform heat generation as a result of distributed long- and short-range interactions. The spatial correlations of these events with the underlying inhomogeneity are found to be nonidentical. Investigation of multiple inhomogeneity fields reveals an exponential scaling of plating severity and early onset in contrast to the homogeneous limit. Anode and cathode inhomogeneities couple nonlinearly to grow peculiar electrodeposition patterns. These mechanistic insights annotate the complex functioning of spatially nonuniform electrodes.

 [DOI: 10.1149/1945-7111/ab8fd7]

Manuscript submitted February 25, 2020; revised manuscript received April 19, 2020. Published May 20, 2020. *This paper is part of the JES Focus Issue on Battery Safety, Reliability and Mitigation.*

Supplementary material for this article is available online

Electromobility potential of batteries[1–4] is assessed in terms of the range (characterized by specific discharge capacity[5]), safety (related to thermal excursion[6,7]), life (defined by degradation modes[8,9]), cold-start (ability to discharge from sub-zero temperatures[10,11]) and fast charging (recharging time comparable to gasoline refueling[12–19]). Electrode engineering[20–25] has improved energy and power densities, while electrolyte modifications[26–28] have helped modulate safety and degradation. Recent advances proffer promising remedies for cold-start.[29–32] On the other hand, the fast charging has been an elusive aspiration,[14–17,33] especially for the futuristic goal of 10 min charge[12]—referred to as Extreme Fast Charge (XFC). Such a high charging rate (6C or equivalent) is essential for battery vehicles to compete with the refueling time of their gasoline counterparts. When Li-ion batteries are operated under these far-from-equilibrium conditions, deleterious interactions are found to multiplicate, engendering reduced energy storage, increased heat generation causing a greater safety concern, and accelerated aging particularly due to lithium plating at anodes.[13,34,35]

The functionality of porous electrodes used in such cells is attributed to reactive—diffusive interactions. Progressively higher currents shorten reactive timescale as more reactions take place in unit time (electrode reactions are proportional to current). XFC represents a fundamental regime shift where reactive timescale is shorter than the diffusive timescale, thus qualifying transport as the limiting interaction (for normal operating currents, diffusive timescale is shorter and equivalently the electrode response is kinetically limited[36,37]). The diffusive transport is an equilibrating influence and acts to smooth out species gradients. XFC operation, given the shorter reaction timescale, provides insufficient relaxation for these gradients. As a result, the aforementioned chemical nonuniformity is prone to amplification.

The diffusive timescale is length-scale dependent, $\gamma_D \sim l^2/D$. The electrochemical response of intercalating electrodes is composed of two diffusive transport mechanisms—lithium intercalation in active particles and ionic distribution in the electrolyte pore network. Since solid-state transport is characteristically slow ($D_a \ll D_e$), ionic concentration gradients are negligible at the pore scale where $\gamma_{D_a} \sim R_p^2/D_a \gg R_p^2/D_e \sim \gamma_{D_e}^{pore}$ (pore size scales with active particle radius for narrow particle size distribution representative of Li-ion electrodes[38]). Further, it can be shown that ionic concentration is locally uniform over a volume element containing a statistically significant amount of particulate matter.[39] This volume is referred to as the Representative Elementary Volume (REV[40–43]; $\gamma_{D_e}^{REV} \sim \ell^2/D_e$). Thus, electrolyte nonuniformity is homogenized at the REV length-scale, ℓ. At larger lengths, e.g., electrode thickness, transport becomes limiting $\gamma_{D_e}^{electrode} \sim L_{electrode}^2/D_e > \gamma_R$ at higher currents (the ratio of diffusive and reactive timescales is more commonly known as Damköhler number[44]). Porous electrodes contain geometrical variability at multiple length-scales, however, only larger than REV scales translate to ionic gradients. In such inhomogeneous electrodes, spatial variability is a three-dimensional feature (Figs. 1a–1b). The inhomogeneities at the particle scale, e.g., carbon-binder network, manifest as short-range interactions, which given their localized nature do not propagate to larger lengths.[36,45–47]

The XFC operation of inhomogeneous electrodes is thus susceptible to nonuniform physicochemical activity (physical field, e.g., temperature; chemical field, e.g., concentration) given the underlying geometrical inhomogeneity and timescale sequencing favoring nonuniformities. The understanding of inhomogeneous electrodes is quite primitive[48–61] with a consensus that heterogeneities negatively affect behavior. In situ experimental techniques that could shed light on the underlying spatial fields are still in their nascent stage,[62–71] with an additional constraint to track fast XFC transients. Alternatively, we combine electrode tomograms and physics-based analysis to investigate the spatiotemporal dynamics resulting from the XFC operation of inhomogeneous electrodes. We find that the inhomogeneities lead to distributed physicochemical activity marked by preferential intercalation, localized lithium plating, and heat spots. The severity of plating is explored with the degree of inhomogeneity. We deconvolve the coupling between the anode and cathode inhomogeneity fields and resultant electrodeposition patterns.

*Electrochemical Society Member.
[a]Present address: Argonne National Laboratory, Lemont, Illinois 60439, United States of America.
[z]E-mail: pmukherjee@purdue.edu

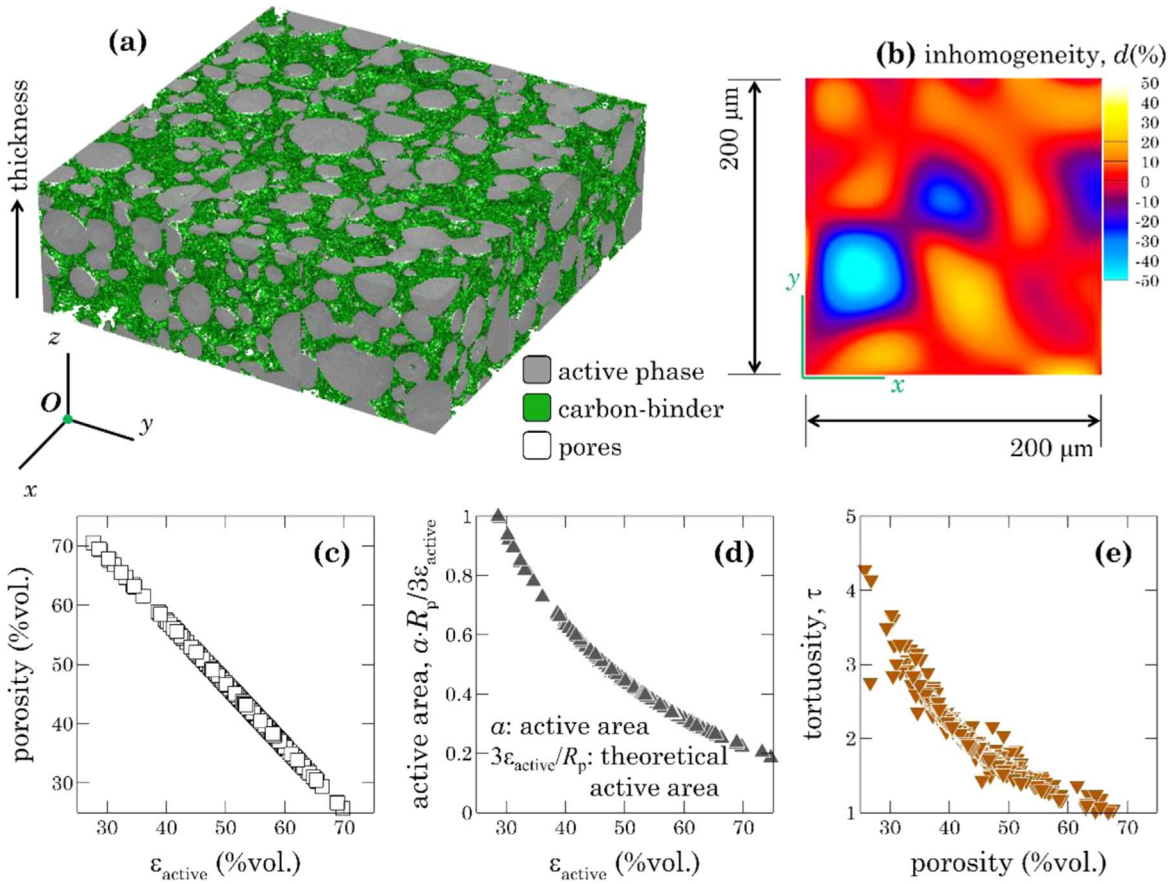

Figure 1. Characteristics of inhomogeneous electrodes: (a) microstructural reconstruction with essential phases in a composite electrode (b) corresponding dimensionless inhomogeneity field, d (c) correlated porosity and active material variation, and equivalent distributions of (d) available active area and (e) tortuosity.

Geometrical Characteristics of an Inhomogeneous Electrode

State-of-the-art lithium battery electrodes are composed of energy storing active phase, carbon particles facilitating electron conduction and polymeric binder ensuring interparticle mechanical connections. Electrolyte occupies the pore network formed due to the porous arrangement of solids. X-ray tomography[72,73] images large enough electrode structure to be useful for identifying inhomogeneity, however, detection of carbon—binder domains (CBD) is ambivalent and segmentation marks electrode domain into active particles and CBD + pore phase. Such segmented information is supplemented via CBD arrangement (arrangement of CBD is based on an understanding of the evaporation dynamics of electrode slurry[36,38,74–77]). Figure 1a demonstrates a schematic reconstruction of a composite electrode with the relevant material phases. Once the REV scale, ℓ, is identified for such a structure[36,38,43,58,78,79] through transport calculations, a dimensionless inhomogeneity field, d, is constructed (refer Section S1). The active material distribution, i.e., the spatial profile of active material volume fraction, is rescaled to obtain the dimensionless d-field. $d = 0$ refers to the electrode averaged active (macroscopic) material content, positive d identifies denser locations, while negative values correspond to active material deficient spots. A representative d-field is shown in Fig. 1b. The dimensionless d-field, thus, decouples inhomogeneity from specific active loading, and groups electrodes with different capacities but identical inhomogeneity.

For a given d-field, electrode specifications help generate corresponding phase distributions (Section S2). The electrode specifications,[22,80–83] e.g., composition, identify electrode averaged phase fractions. For the homogeneous electrodes, these specifications are the same for every spatial location. On the other hand, for the inhomogeneous electrodes, one needs additional information of spatial variability, that is codified as the d-field. Once phase fraction maps are available (Fig. 1c), property correlations (relevant for composite Li-ion battery electrodes[36,37,45,84]) consistently create effective property statistics (Figs. 1d–1e). Here we fix the electrode compositions (Graphite anode with 94: 4: 2 and NMC cathode with 90: 5: 5—active: binder: carbon by wt.), capacities (3.0 mAh cm^{-2} cathode and loading ratio N/P = 1.1) and thicknesses (both 75 μm) to be relevant for current XFC baseline.[13,35,85,86] Different inhomogeneity fields are considered to discern spatial correlations of physicochemical dynamics and underlying inhomogeneity.

CBD arrangement at the active particle surface is governed by surface energies and capillarity of the evaporating slurry.[83,87] A denser active packing attracts more CBD given the greater particle surface area per unit volume (Section S2). In turn, pockets of high active fraction exhibit smaller porosities and vice versa (Fig. 1c). The presence of CBD partially covers the active particle surface and reduces active material—electrolyte contact (electrochemical reactions take place at this interface). As aggregates of active particles signify stronger CBD localization, they experience a higher reduction in active surface (Fig. 1d). CBD also distorts the pore network, resulting in a more convoluted pore network as is evident from higher tortuosities in Fig. 1e. The cathode has a greater amount of CBD (for the presently considered recipes, the cathode has about twice the volume of CBD compared to anode[45]) and subsequently, these deleterious effects are more pronounced.

Typically graphite anodes are made up of platelet-like particles that exhibit higher tortuosities.[38,45,49,88] Since XFC is a transport-limited operation, spherical graphite morphology is preferred to decrease the transport resistance.[13,86] Accordingly, the present analysis employs spherical active particles for both the electrodes

and tomograms are used to extract inhomogeneity fields (section S1). The dimensionless inhomogeneity fields are combined with electrode specifications (e.g., carbon/binder content, N/P ratio, etc.) to reproduce 3D distributions of active material, carbon-binder domains and electrolyte-filled pores for each of the electrodes. These phase fractions are further used to describe the variation of relevant effective properties,[36] namely, active area, pore tortuosity and electronic conductivity (section S2).

Evolution of Physicochemical Fields

The extreme fast charging of Li-ion cell with prescribed electrode inhomogeneities is simulated (Section S3) from a nearly discharged state (3.0V) to a voltage cutoff of 4.2V at a 6C rate (for a 3.0 mAh cm^{-2} capacity cell this amounts to a charging current of 18 mA cm^{-2}). A scaled outline of the cell is shown in Fig. 2a along with the eletrolyte concentration distribution at the end of charge. During charging cathode delithiates and anode lithiates. Equivalently, ionic flux is directed from cathode to anode and gradually smaller Li^+ concentrations are found (Fig. 2a). Fingerprints of inhomogeneity (Fig. 1b) are apparent on the ionic distribution and more clearly on the concentration isocontour as shown in Fig. 2a.

The cathode is first kept homogeneous, while the anode is assigned the most inhomogeneous field from the database Fig. S2 and Table SI (available online at stacks.iop.org/JES/167/090542/mmedia). As a result, the cathode concentration field is relatively uniform in the electrode plane. Table I identifies the different cells discussed herein. All have identical electrode capacities and only differ in terms of the inhomogeneity fields.

Macroscopic (Section S4) evolutions are presented in Fig. 2b. The abscissa represents a scaled charging capacity (normalized using cell capacity). At a high charging rate of 6C, the charging capacity is less than half of the theoretical capacity. Two plating indicators (Section S4) are tracked to offer global trends. Lithium electrodeposition is identified by the electrochemical reaction:

$$Li \underset{\text{deposition}}{\overset{\text{dissolution}}{\rightleftharpoons}} Li^+ + e^- \qquad [1]$$

Here Li refers to plated lithium at graphite—electrolyte interface, while Li^+ relates to local ionic concentration in the electrolyte and e^- are the electrons in the graphite. Appropriate kinetic expression[89] for lithium plating on graphite is

$$i_P = i_P^0 \{ e^{(1-\alpha)F(\phi_{anode}-\phi_{electrolyte}-U_P)/RT} - \left(\frac{c_e}{c_e^0}\right) e^{-\alpha F(\phi_{anode}-\phi_{electrolyte}-U_P)/RT} \}$$

where i_P^0 and U_P are independent of concentration. U_P identifies the thermodynamic (equilibrium) potential for Li deposition on the working electrode against the Li/Li^+ counter electrode at reference concentration ($c_e^0 = 1000$ mol m^{-3}), and by definition, $U_P = 0$ V. (Alternatively, the concentration dependence can be clubbed in exchange current density and equilibrium potential to arrive at an equivalent expression; herein above expression with constant properties is used given a more straightforward interpretation.) Thus, the surface plating current is expressed as (per unit active area):

$$i_P = i_P^0 \{ e^{(1-\alpha)F(\phi_{anode}-\phi_{electrolyte})/RT} - \left(\frac{c_e}{c_e^0}\right) e^{-\alpha F(\phi_{anode}-\phi_{electrolyte})/RT} \} \qquad [2]$$

Since graphite is a good electron conductor,[90] electronic transport does not limit lithium plating and ϕ_{anode} is spatially uniform. Consequently, any spatial variation in plating current is related to gradients in electrolyte potential, $\phi_{electrolyte}$ and Li^+ concentration. In other words, the necessary driving force is the (local) overpotential, $\eta_P = \phi_{anode} - \phi_{electrolyte}$. However, not all favorable (i.e., negative) overpotentials result in electrodeposition. Local ionic availability is an additional prerequisite.

Conventional studies using three-electrode cells (e.g.,[91]) operate at relatively moderate currents where ionic gradients are not severe and negative overpotentials synonymize electrodeposition. Thus, negative overpotentials are often argued to represent lithium plating. On the other hand, for XFC considerable ionic depletion takes place —even close to anode surface—and consequently, actual electrodeposition events are delayed until more negative overpotentials are achieved. Such a delayed deposition has been recently observed for fast charging conditions.[92] The occurrence of negative overpotentials is followed in terms of the dimensionless driving force, ϕ^* (Eq. 3), while quantitative information is revealed by a severity descriptor, π^* (Eq. 4). Here Γ_{anode} is the total anode active area (= active area × electrode volume).

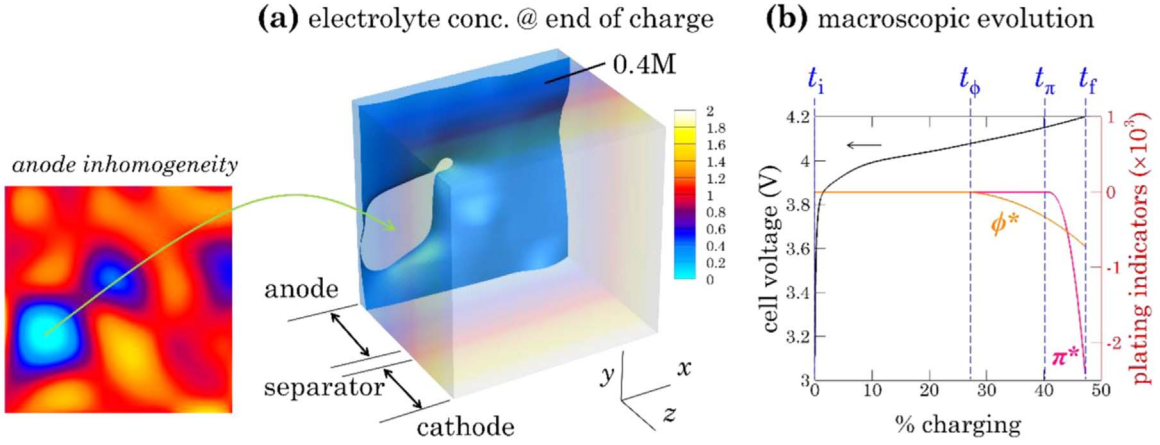

Figure 2. Extreme fast charge (6C till 4.2V) of graphite (anode)—NMC333 (cathode) cell: (a) end of charge ionic concentration (molar) distribution in the cell (b) temporal dynamics of cell voltage, plating activation, ϕ^*, and electrodeposition severity, π^*. Presence of electrode inhomogeneities translates to nontrivial concentration distribution as revealed by the concentration isocontour in (a). Corresponding anode inhomogeneity field is shown in the inset. At such high rates, electrodeposition does not immediately start when activation overpotential is available since locally ions are partially depleted due to high charging currents. The initial electrolyte concentration is 1.2M. $t_i = 0$ is the start of charging; t_ϕ refers to the time beyond which potentials are favorable for plating; t_π marks the onset of plating and t_f records the end of charging. If electrolyte concentration, i.e., Li^+, were nearly uniform, favorable potentials immediately trigger plating and $t_\phi \approx t_\pi$. However, at higher currents, appreciable gradients exist in the electrolyte and delays the onset of plating.

Table I. Electrode inhomogeneities for the examples discussed here. For all calculations, the cell specifications are identical and refer to the XFC baseline[13,86]: 3 mAh cm^{-2} cathode, N/P = 1.1, $L_{cathode} = L_{anode} = 75\ \mu$m, cathode composition 90: 5: 5 by wt. and anode is 94: 4: 2 by wt.

Figure	Anode	Cathode
2	inhomogeneous (structure "n" in Fig. S2 and Table SI)	homogeneous
3	same as Fig. 2	
4	inhomogeneous (structures from Fig. S2 and Table SI)	homogeneous
5	homogeneous anode—homogeneous cathode	
	inhomogeneous anode (structure "n")—homogeneous cathode	
	inhomogeneous anode (structure "n")—inhomogeneous cathode (parageneous)	
	inhomogeneous anode (structure "n")—inhomogeneous cathode (diageneous)	

$$\phi^* = \frac{1}{t_{\text{theoretical}}\,\Gamma_{\text{anode}}} \int_{t_{\text{operation}}}^{0} \left\{ \int_{\Gamma_{\text{anode}}} (\phi_{\text{anode}} - \phi_{\text{electrolyte}})\, d\Gamma \right\} \text{d}t \qquad [3]$$

when $\phi_{\text{anode}} < \phi_{\text{electrolyte}}$

$$\pi^* = \frac{1}{t_{\text{theoretical}}\,\Gamma_{\text{anode}}} \int_{t_{\text{operation}}}^{0} \left\{ \int_{\Gamma_{\text{anode}}} \left(1 - \left(\frac{c_e}{c_e^0} \right) e^{-F(\phi_{\text{anode}} - \phi_{\text{electrolyte}})/RT} \right) d\Gamma \right\} \text{d}t \qquad [4]$$

when $\phi_{\text{anode}} < \phi_{\text{electrolyte}}$

The delayed electrodeposition is apparent from noncoincident onsets for ϕ^* and π^* in Fig. 2b. Notice that Eqs. 3 and 4 follow from the kinetic expression (Eq. 2). Given the ambiguity[93–96] in reported plating exchange current, i_{p}^0 and charge transfer coefficient, α, the descriptors ϕ^* and π^* are expressed in dimensionless forms to retain their validity.

Implication I: A noteworthy plating characteristic of fast charging is electrodeposition before even 50% charging, unlike normal charging where plating takes place towards the end of charge.[45,97–99] Given this difference, traditional charging strategies, e.g., CC-CV charge, fall short of preventing lithium plating during XFC.

Local evolutions are plagued by anode inhomogeneities as delineated in intercalation (Fig. 3a), electrodeposition (Fig. 3b) and heat (Fig. 3c) maps for anode surface, i.e., anode—separator interface, at the end of charging. The temporal evolution of electrodeposition, both at the anode surface and propagation of plating fronts in the bulk of anode, is introduced in Movie S1. The spatial nature of the distributions in Figs. 3a–3c) is nonidentical, suggesting elemental differences in underlying mechanisms.

A comparison of the intercalation profile (Fig. 3a) with active material distribution (Fig. 3j) indicates a strong one—to—one correlation. Lowest active material locations experience the highest intercalation (Fig. 3a reports lithium content at the active particle surface at each spatial location; average lithiation in these particles is less than the corresponding surface value during charging). Recall that active material aggregates attract more CBD and in turn suffer from the reduced active area and increased transport resistance (Figs. 1d–1e). Thus, the ionic flux preferentially diverts to lower active packing locations that offer relatively smaller resistance to reactions (more active area Fig. 1d) and transport (higher porosity and smaller tortuosity; Fig. 1e). This ordering reflects in reaction distribution at the start of charging, t_{i} (Fig. 3d) resulting in preferential intercalation. Gradually, as these locations lithiate, their resistance to intercalation increases and the ionic flux coming from cathode partially reroutes to higher active packing locations. Such a transition is apparent in Fig. 3d where reaction distribution successively peaks at different locations, all the while preferentially filling less resistive spots (Fig. 3g; the time stamps correlate to representative features in Fig. 2b). As a result, the intercalation profile mimics the electrode inhomogeneity. Qualitatively similar behavior is observed in other recent studies examining inhomogeneous electrodes.[55,58,59]

A close examination of the electrodeposition profile (Fig. 3b) discloses a quadratic trend where the least dense and most dense locations experience relatively less severe plating as compared to intermediately packed regions. Since electrodeposition events relate to ionic concentration and local activation, their time evolutions are plotted in Figs. 3e and 3h respectively for the time interval $[t_\phi, t_{\text{f}}]$. Overpotential buildup $[t_\phi, t_\pi)$, plating onset, t_π, and deposition $(t_\pi, t_{\text{f}}]$ are colored differently to aid visual inspection. Note that t_ϕ and t_π mark the leading occurrences of negative overpotential and electrodeposition, respectively.

The evolution of electrochemical fields is dominated by intercalation since lithium plating is a secondary (side) reaction. As preferential intercalation takes place at lower active material locations, the local ionic concentration drops to create necessary gradients for densely packed locations to provide reactants. On the other hand, very densely packed locations are deprived of ions given their higher transport resistances. Thus, extremum spots observe lower ionic concentrations (Fig. 3e). Equivalently, electrolyte potential, $\phi_{\text{electrolyte}}$, also drops at these extremum positions to channelize ionic current.

Due to the high electronic conductivity of graphite, anode potential has negligible gradients, i.e., $\phi_{\text{anode}}(x, y, z, t) \approx \phi_{\text{anode}}(t)$. As a consequence, activation overpotential, $\eta_{\text{P}} = \phi_{\text{anode}} - \phi_{\text{electrolyte}}$, is smaller (in magnitude) at extremum points and higher at intermediate active material densities (Fig. 3h).

Since local plating (Eq. 2) is jointly defined by overpotential, $\eta_{\text{P}} = \phi_{\text{anode}} - \phi_{\text{electrolyte}}$ (Fig. 3h: most negative at moderate active packings) and ionic concentration (Fig. 3e: higher at moderate packings), the resultant plating is more severe at intermediate locations (Figs. 3b, 3k). Such a sequencing maintains over time as is discernible from the leftward leaning point cloud at each timestamp (Fig. 3k). Thus, more plating takes place at moderately dense locations. If both the electrodes were homogeneous, each lateral point at identical thickness has similar ionic concentration and leads to a uniform electrodeposition pattern, resulting in less severe and delayed plating in homogeneous electrodes (subsequently discussed in Fig. 4a). Note that the electrodeposition pattern in Fig. 3b plots localized plating severity $\text{d}\pi^*$ (Eq. (S27)) normalized to highest local plating, i.e., $\text{d}\pi^*/\text{d}\pi^*_{\text{max}}$.

Local heat accumulation, $\text{d}Q$(Eq. (S32)) exhibits a spatial dependence (Fig. 3c) that is distinct from intercalation (Fig. 3a)

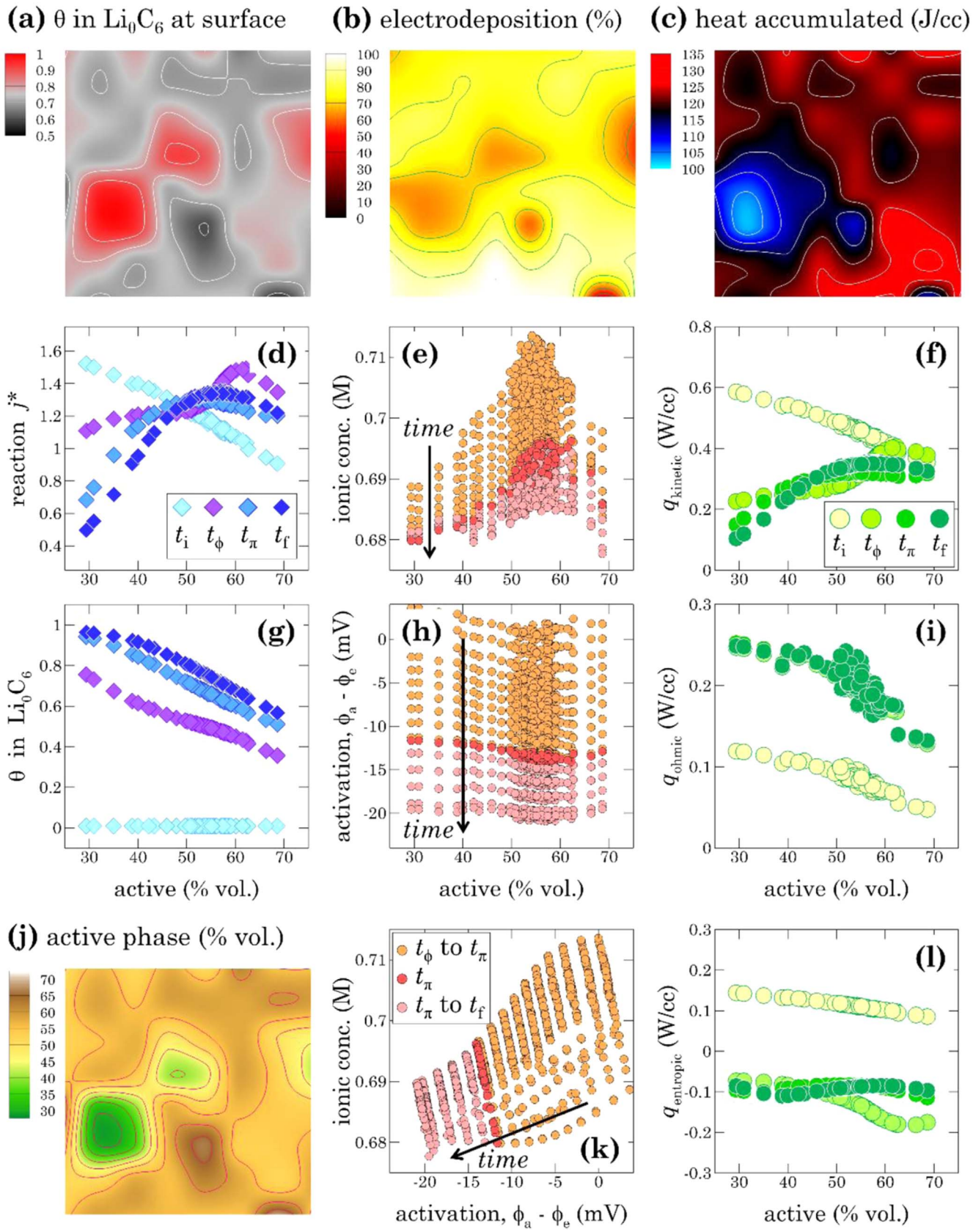

Figure 3. (a) Intercalation, (b) electrodeposition and (c) heat generation at the anode—separator interface at the end of charging (before rest) are a result of evolving elemental interactions (d) electrochemical reaction (e) ionic concentration (f) kinetic heat (g) intercalated lithium (h) activation overpotential for lithium plating (i) ohmic heat (k) ionic concentration vs. plating activation and (l) entropic heat. (j) Active material distribution is shown alongside to highlight the spatial correlations for (a) intercalation (b) plating and (c) heat accumulation maps. The field of view is 200 × 200 μm^2. j^* quantifies the scaled reaction current; θ is normalized intercalated lithium at the anode; ϕ_a is anode potential; ϕ_e is local electrolyte potential; $q_{kinetic}$, $q_{transport}$, $q_{entropic}$ are local volumetric heat generation rates.

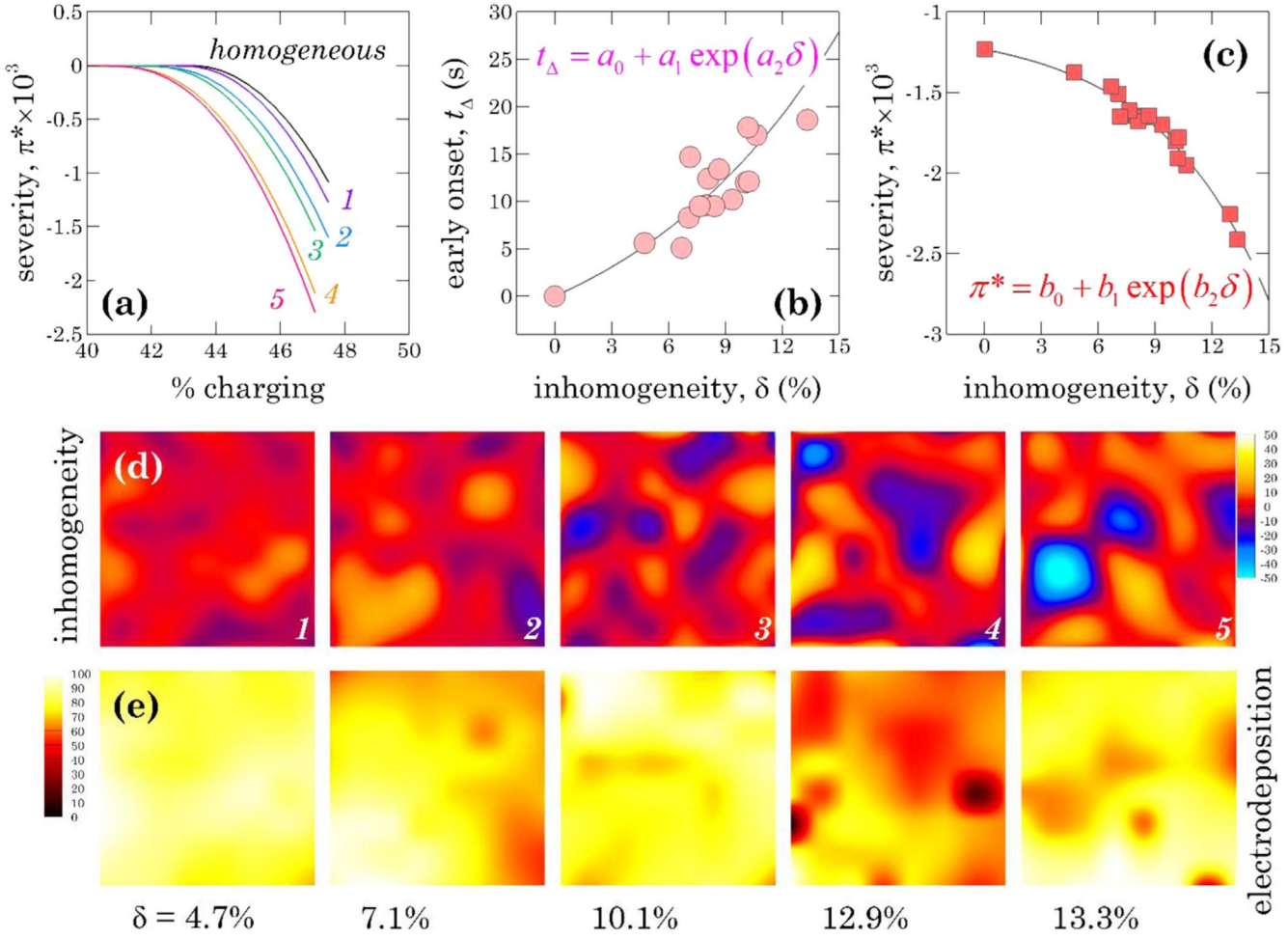

Figure 4. Correlating spatiotemporal electrodeposition with anode inhomogeneity (cathode is kept homogeneous to isolate anode features): (a) evolution of electrodeposition (b) early plating onset in the presence of inhomogeneity (c) severity—inhomogeneity scaling (d) corresponding anode inhomogeneity maps (labeled in an increasing order of their inhomogeneity indices) and (e) electrodeposition patterns at the end of 4.2V charge at 6C.

and electrodeposition (Fig. 3b) patterns. Less packed locations have smaller total heating, the highest heating is observed at intermediate densifications and somewhat reduced heating at highly dense locations. Total heating is composed of three elemental contributions. Kinetic heating (Fig. 3f) $q_{\text{kinetic}} = j\eta$ relates to local reactions (Eq. (S29)). The reaction overpotential, η, scales positively with (j/ai_{l}^{0}). Hence, the kinetic heat map (Fig. 3f) resembles the reaction evolution (Fig. 3d). The exchange current density, i_{l}^{0} (Eq. 5) increases with lithiation, in turn decreasing overpotential. As a result, kinetic heat values scale down as charging progresses in Fig. 3f.

$$i_I^0 = kc_{\text{anode}}^{\max}\sqrt{c_{\text{e}}\,\theta^{\text{surf}}(1-\theta^{\text{surf}})} \qquad [5]$$

Ohmic heating (Eq.(S30)) collectively depends on local currents (ionic and electronic) as well as associated resistances. The transport resistance monotonically increases with active material content (i.e., decrease in porosity[22,38,82,100]), while ionic current shows an opposite dependence. Given a squared dependence on current, ohmic heating qualitatively follows current distribution (Fig. 3i). Electronic current has a negligible contribution given the high conductivity of solid composites. Over time ionic concentration at anode decreases, which increases the resistance, resulting in higher ohmic heating[45] as shown in Fig. 3i. The ionic concentration profile becomes quasi-steady after initial transients, and in turn, late time data are closely grouped in Fig. 3i.

The third contribution is due to entropic heat (Eq. S31) that signifies the thermodynamic penalty for heat—to—work conversion. $q_{\text{entropic}} = -jT(\partial U/\partial T)$ contains reaction, j, and material property, $\partial U/\partial T$, dependencies. As a result, entropic heat profiles exhibit qualitative similarity (Fig. 3l) to reaction evolution (Fig. 3d). The entropic coefficient, $\partial U/\partial T$, varies with the extent of lithiation, θ. Both jointly give rise to the specific variations in Fig. 3l. For fast operation, irreversible heat generations (kinetic and ohmic) dominate the thermal metastability.[101–103] As is evident from Figs. 3f and 3i, the kinetic heat gradually decreases in time, while ohmic heat increases. Initially, both the heating contributions are localized in low active material regions. However, at late times, the spatial correlation of kinetic heat reverses (Fig. 3f). The opposite spatial nature of kinetic and ohmic heats give rise to the nonlinear heat accumulation (Fig. 3c).

As reactions and concentrations are interrelated, heat generation causes temperature rise. The nonuniform heat generation may result in inhomogeneous temperature. As mentioned earlier, diffusion acts to smooth out concentration gradients. Equivalently, thermal conduction accounts for the temperature build-up. When thermal conduction is slow compared to the timescale of heat accumulation, it results in nonuniform temperature. On the other extreme, the temperature is spatially uniform. For typical battery materials,[104,105] thermal diffusivity, $k/\rho C \sim \mathcal{O}(10^{-6}\ \text{m}^2\ \text{s}^{-1})$, while diffusion, $D_{\text{e}} \sim \mathcal{O}(10^{-10}\ \text{m}^2\ \text{s}^{-1})$ is much slower. Thus, for comparable lengths, thermal time constant is much smaller compared to the diffusion

time, and one at the lengths considered here, the nonuniform heat generation does not cause appreciable temperature gradients. The thermal inhomogeneity becomes relevant at larger lengths where conduction timescale, $\gamma_c \sim L^2/(k/\rho C)$, is larger. Such timescale differences justify why concentration inhomogeneity[70] is observed at smaller lengths (~10 s of microns) while temperature nonuniformity[106,107] manifests at macroscopic dimensions (~mm and above).

Electrodeposition Scales with Inhomogeneity

Lithium plating in graphite anodes represents a degradation mechanism, thus characteristically differing from electrodeposition on lithium metal electrodes[108–113] where it is responsible for reversible energy storage. Electrodeposition scaling with electrode inhomogeneity is examined in Fig. 4. Five illustrative inhomogeneity profiles (Fig. 4d) are shown. Note that all anodes have identical total capacities. These *d*-profiles are also annotated on the inhomogeneity database (Table SI) and reflect progressively increasing inhomogeneity (quantified by inhomogeneity index, δ; Fig. 4d). Macroscopic evolution of deposition severity (Fig. 4a) reports earlier plating onset, t_Δ, as well as intensified degradation, π^*. The examination of final deposition patterns (Fig. 4e) highlights the previously discussed quadratic trend showing the highest deposition at intermediate active material densification. Fig. 4e) also exemplify vanishing plating nonuniformity in the homogeneous limit. Similarly, remaining inhomogeneity profiles from the database (Fig. S2) are explored to quantify electrodeposition—inhomogeneity scaling in terms of early onset (Fig. 4b) and plating severity (Fig. 4c). Both exhibit exponential dependence on inhomogeneity:

$$t_\Delta = a_0 + a_1 \exp(a_2 \delta) \quad [6]$$

$$\pi^* = b_0 + b_1 \exp(b_2 \delta) \quad [7]$$

The exponential nature makes inhomogeneities particularly detrimental. Table II illustrates the critical role of inhomogeneities in lithium plating. An electrode with 14% inhomogeneity experiences twice severe plating as well as plating onset is 24 s (about half a minute) earlier than the homogeneous response. However, subsequently, severity doubles with approximately half as much inhomogeneity (Table II). Concurrently, early onset duration grows. In addition to leading to spatially nonuniform deposits, inhomogeneities accelerate degradation. Approximately 23% inhomogeneity causes six times severe electrodeposition and plating commences about a minute earlier, which is a considerable miscalculation for a less than ten minutes operation. Smaller inhomogeneities ($\delta < 5\%$) exhibit approximately linear scaling in Figs. 4b–4c and could be justified as acceptable.

Implication II: Battery management systems (BMS) employing a physics-based control[114,115] make decisions for homogeneous electrodes. Such an approach underpredicts the plating onset, thus considerably delaying execution during XFC.

Implication III: BMS relies on cell level (macroscopic) measurements for decision making. Such measurements do not convey necessary information regarding inhomogeneities and should be relied on with caution.

Implication IV: Potentiostat-driven experiments[91,92,116,117] such as three-electrode cell studies are sensitive to probe size and location given the noncanonical interactions in XFC of inhomogeneous electrodes.

The transport limited nature of XFC qualifies active particle morphology with smaller tortuosity[38,54] as a preferred choice. Microstructure analysis suggests that spherical particles are best suited for reduced tortuosity for similar electrode recipes. Hence, the present investigation revolves around spherical active particles. An alluring possibility is to employ straight ion channels to reduced electrode effective tortuosity.[25,85,118] However, such electrodes are highly inhomogeneous and would lead to accelerated aging. For such electrodes, inhomogeneity is affected by channel size as well as channel number density.

Implication V: Reduction in electrode tortuosity at the cost of inhomogeneity (e.g., dual-porosity electrode structures[25]) ends up being detrimental to XFC given the inhomogeneity—electrodeposition scaling.

Communication between Anode and Cathode Inhomogeneities

Extreme reactivity and metallic nature of (freshly deposited) lithium have equivocated its explicit quantitative characterization, save for some recent advances.[62,93,117,119–122] Most of these techniques are usually inferential and/or provide macroscopic measures. On the other hand, lithium plating reaction (Eq. 1) is fundamentally a short-range interaction. During fast charging, anode activity is further constrained by ionic flow from the cathode. Such an upstream dependency could further complicate the spatiotemporal evolution of electrodeposition patterns. Figure 5 interrogates the effect of upstream perturbances resulting from cathode inhomogeneities. Earlier discussions (Figs. 3 and 4) relied on the homogeneous cathode that is expected to (ideally) provide uniform ionic flux.

For a given anode inhomogeneity, two extremes of cathode inhomogeneity can be conceived

i. completely aligned *d*-fields where inhomogeneity peaks and valleys coincide in the electrode plane and
ii. a case of perfect misalignment that matches each peak with a valley of equivalent geometrical attributes.

The aligned combination results in *d*-fields being mirror images of each other, while the anti-aligned situation results in cathode *d*-field being a negative image of the anode *d*-field. Borrowing the dipole alignment terminology from magnetism,[123] the aligned cathode is referred to as parageneous (Fig. 5h), while the anti-aligned cathode is denominated as diageneous (Fig. 5l).

Figures 5a–5c present electrodeposition patterns at the end of charge for these three situations. Despite anode inhomogeneity being identical in Figs. 5a–5c, electrodeposition patterns are conspicuously different. To discern the origins of spatial correlations, ionic fluxes at the anode (Figs. 5e–5g) and cathode (Figs. 5i–5k) surfaces are compared at the end of charge. Currents are completely ionic at both of these interfaces. Figure 5e exhibits the localization of ionic flux as expected from preferential intercalation (Figs. 3a, 3e). Given the thinness of separator, ionic current leaving cathode has to partly align to anode inhomogeneity, resulting in a slightly nonuniform

Table II. Plating severity for different anode inhomogeneities.

$\pi^*/\pi^*_{\text{homogeneous}}$	Inhomogeneity, δ (%)	Relative inhomogeneity increase, $\Delta\delta$ (%)	Early onset, t_Δ (s)	Relative shift in early onset, Δt_Δ (s)
1	0	—	0	—
2	13.7	13.7	~24	24
4	19.8	6.1	~48	24
6	22.8	3	~65	17
8	24.7	1.9	~79	14
10	26.2	1.5	~91	12

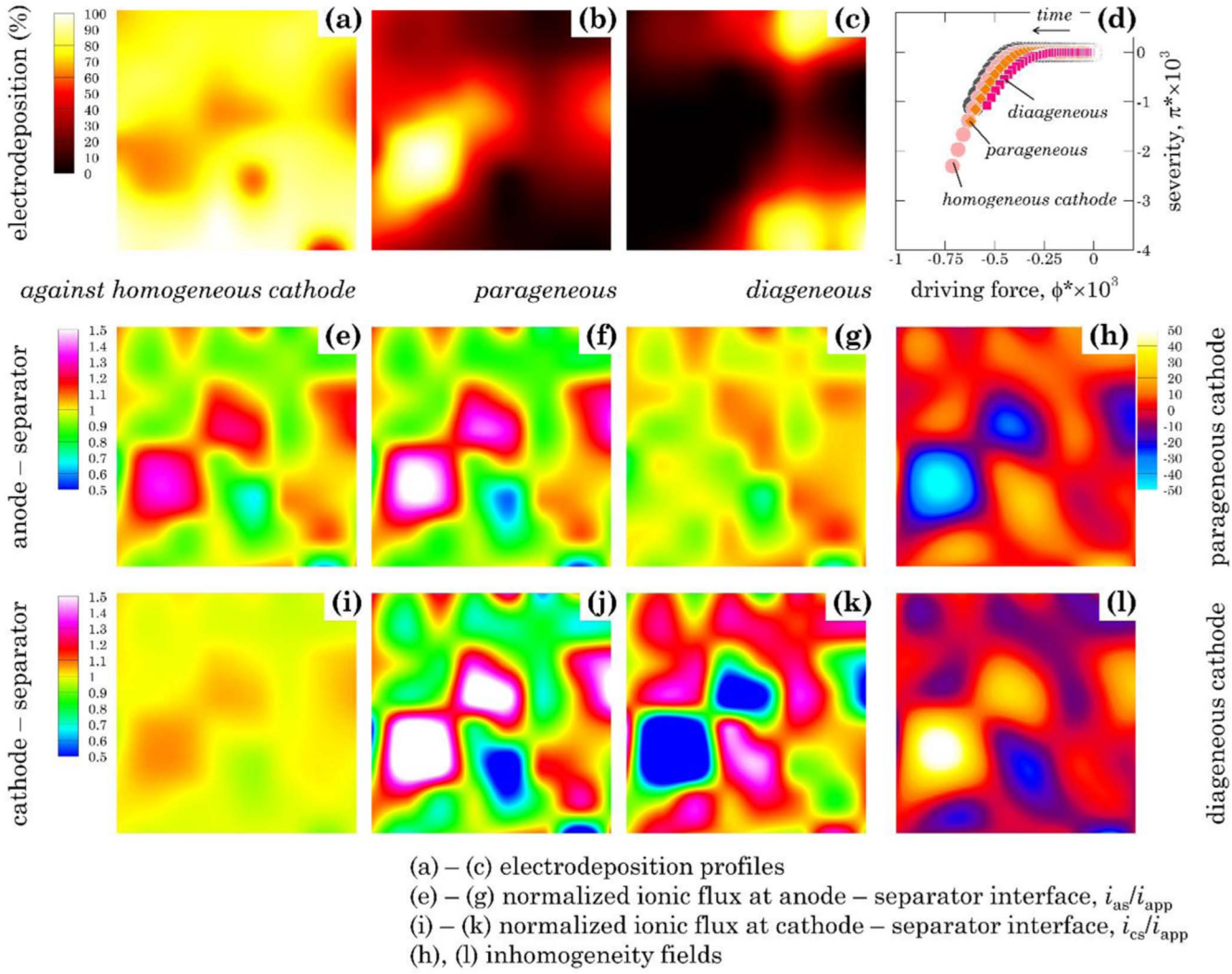

Figure 5. Coupling of anode and cathode inhomogeneities: (a)–(c) electrodeposition patterns at the end of charge for inhomogeneous anode—homogeneous cathode, diageneous cathode, and parageneous cathode combinations, respectively. A parageneous cathode (h) has an inhomogeneity field aligned to the anode, while a diageneous cathode (l) has a completely anti-aligned inhomogeneity field. (d) Time evolution of electrodeposition severity, π^*, against plating driving force, ϕ^*; homogeneous anode—homogeneous cathode data is also sketched for comparison (background dark circles). Normalized ionic flux, $i^* = i/i_{app}$ at anode—separator (e)–(g) and cathode—separator (i)–(k) interfaces at the end of charge.

current distribution at the cathode surface (Fig. 5i). On the other hand, for the parageneous cathode, the current leaving cathode (Fig. 5j) is aligned to the anode reaction spots. Such aggravated current localization fosters coincident electrodeposition (Fig. 5b). The diageneous cathode biases the outgoing ionic flux (Fig. 5k) towards high resistance pockets in the anode. Such a mismatch causes a cross-flow near the anode surface, partially diluting the current inhomogeneity at the anode surface (Fig. 5g). As a result, the electrodeposition pattern is much convoluted (Fig. 5c).

Implication VI: In a real setting, there is little control over tuning and aligning electrode inhomogeneities. Consequently, the electrodeposition pattern exhibits spatial features of each of these scenarios (to varying extents) such that observed electrodeposition might seem probabilistic.

Implication VII: Given this cross-talk between the two electrodes through the ionic field, it is not sufficient to homogenize anode. A homogeneous anode paired up with an inhomogeneous cathode would still exhibit localized plating.

Figure 5d differentiates global plating dynamics on a severity—activation map for the different inhomogeneity pairs. Additionally, the temporal response of the homogeneous—homogeneous pair is also sketched in the background (dark circles). Departure from the horizontal trend marks the electrodeposition onset, i.e., t_π. Inhomogeneity leads to increased resistance and as a result earlier onset. Aligned inhomogeneities (parageneous cathode) exhibit a smaller resistance as compared to the anti-aligned inhomogeneities (diageneous cathode). Hence, plating onset is earliest with a diageneous cathode.

The electrodeposition patterns discussed here (e.g., Fig. 5a) provide insights into electrodeposition preference of lithiating graphite particles that are far apart for electrolyte gradients. Neighboring particles have fairly identical ionic fields and experience similar plating. Note that the morphology of lithium deposits is dictated by interfacial interactions such as crystallinity of graphite—electrolyte wetting and the presence of additional phases (CBD, predeposited lithium, etc.). Non-spherical particle morphology can exacerbate inhomogeneity by altering intercalation response at particle-scale[124,125] as well as increasing pore transport resistance.[38,45,88] Additional complications can arise from multi-phase intercalation behavior of graphite[126,127] and mechanical strains[55,59,128] but have not been considered here.

The present discussion outlines the microscopic details of the first XFC charge. As the cell is cycled, further complexities manifest. Cyclable lithium inventory decreases as more and more lithium plates. Over time, this would decrease the local porosity and alter the reaction distribution. For an initial couple of cycles when the

electrode microstructure has not changed much, the results presented here are directly applicable. For subsequent cycles when plated lithium represents an appreciable contribution and locally decreases porosity, the coupling of electrochemical effects is to be reexamined.

Conclusions

Extreme fast charging (XFC; 6C or equivalent) of lithium batteries designates a fundamental shift from reaction-limited to the transport-limited regime. Diffusive transport is a homogenizing influence. Given its inadequacy during XFC, physicochemical heterogeneities are prone to grow in an uncontrolled fashion. We investigate redox activity in inhomogeneous electrodes under such unstable conditions.

- Electrode-scale inhomogeneities give rise to preferential intercalation, localized plating and heat spots, each with their distinct spatial signatures. Electrode regions densely packed with active material comparatively experience smaller intercalation since they exhibit greater resistance to intercalation as well as ionic transport. Alternatively, moderately packed locations experience more plating (against a homogeneous cathode). As heat generation is made up of three distinct contributions (kinetic, ohmic and entropic) and each of these scales differently, the heat map scales nonlinearly with local active packing.
- Inhomogeneous anodes experience more severe and accelerated electrodeposition as compared to their homogeneous counterparts. The severity and early onset scale exponentially with the degree of inhomogeneity.
- Both anode and cathode inhomogeneities contribute to nonuniform plating. Cathode inhomogeneity biases the ionic flux arriving at the anode, while anode inhomogeneity affects both distribution of incoming ionic flux as well as preferential intercalation (relates to negative potential). Based on the inhomogeneities in both the electrodes and their mutual alignment, resultant electroplating patterns exhibit complex spatial correlation to the inhomogeneities and may appear probabilistic at a cursory observation.
- Such high rates (e.g., 6C) partially deplete anode of lithium ions, thus leading to a delayed plating onset even after negative anode potentials.

The complex interactions arising from the fast dynamics of inhomogeneous electrodes make XFC a scientific challenge, not just an engineering one.

Acknowledgments

Funding provided by the U.S. DOE Office of Vehicle Technology Extreme Fast Charge Cell Evaluation of Lithium-Ion Batteries (XCEL) Program, program manager Samuel Gillard, is gratefully acknowledged. This work was co-authored by the National Renewable Energy Laboratory, operated by Alliance for Sustainable Energy, LLC, for the U.S. Department of Energy (DOE) under Contract No. DE-AC36-08GO28308. The views expressed in the article do not necessarily represent the views of the DOE or the U.S. Government. The U.S. Government retains and the publisher, by accepting the article for publication, acknowledges that the U.S. Government retains a nonexclusive, paid-up, irrevocable, worldwide license to publish or reproduce the published form of this work or allow others to do so, for U.S. Government purposes.

ORCID

Aashutosh Mistry https://orcid.org/0000-0002-4359-4975
Francois L. E. Usseglio-Viretta https://orcid.org/0000-0002-7559-8874
Andrew Colclasure https://orcid.org/0000-0002-9574-5106
Kandler Smith https://orcid.org/0000-0001-7011-0377
Partha P. Mukherjee https://orcid.org/0000-0001-7900-7261

References

1. O. Gröger, H. A. Gasteiger, and J.-P. Suchsland, "Review—electromobility: batteries or fuel cells? " *J. Electrochem. Soc.*, **162**, A2605 (2015).
2. U. Eberle and R. Von Helmolt, "Sustainable transportation based on electric vehicle concepts: a brief overview." *Energy Environ. Sci.*, 689 (2010).
3. X. G. Yang and C. Y. Wang, "Understanding the trilemma of fast charging, energy density and cycle life of lithium-ion batteries." *J. Power Sources*, **402**, 489 (2018).
4. M. Armand and J. M. Tarascon, "Building better batteries." *Nature*, **451**, 652 (2008).
5. J. Betz, G. Bieker, P. Meister, T. Placke, M. Winter, and R. Schmuch, "Theoretical versus practical energy: a plea for more transparency in the energy calculation of different rechargeable battery systems." *Adv. Energy Mater.*, **9**, 1803170 (2019).
6. R. Spotnitz and J. Franklin, "Abuse behavior of high-power, lithium-ion cells." *J. Power Sources*, **113**, 81 (2003).
7. T. M. Bandhauer, S. Garimella, and T. F. Fuller, "A critical review of thermal issues in lithium-ion batteries." *J. Electrochem. Soc.*, **158**, R1 (2011).
8. J. Vetter, P. Novák, M. R. Wagner, C. Veit, K. C. Möller, J. O. Besenhard, M. Winter, M. Wohlfahrt-Mehrens, C. Vogler, and A. Hammouche, "Ageing mechanisms in lithium-ion batteries." *J. Power Sources*, **147**, 269 (2005).
9. M. R. Palacín and A. De Guibert, "Batteries: why do batteries fail ? " *Science (80-.).*, **351**, 1253292 (2016).
10. E. J. Plichta, M. Hendrickson, R. Thompson, G. Au, W. K. Behl, M. C. Smart, B. V. Ratnakumar, and S. Surampudi, "Development of low temperature li-ion electrolytes for NASA and DoD applications." *J. Power Sources*, **94**, 160 (2001).
11. S. S. Zhang, K. Xu, and T. R. Jow, "The low temperature performance of Li-ion batteries." *J. Power Sources*, **115**, 137 (2003).
12. C. Michelbacher et al., "Enabling fast charging—introduction and overview." *J. Power Sources*, **367**, 214 (2017).
13. A. M. Colclasure, A. R. Dunlop, S. E. Trask, B. J. Polzin, A. N. Jansen, and K. Smith, "Requirements for enabling extreme fast charging of high energy density li-ion cells while avoiding lithium plating." *J. Electrochem. Soc.*, **166**, A1412 (2019).
14. S. Ahmed et al., "Enabling fast charging—a battery technology gap assessment." *J. Power Sources*, **367**, 250 (2017).
15. M. Keyser et al., "Enabling fast charging—battery thermal considerations." *J. Power Sources*, **367**, 228 (2017).
16. A. Meintz et al., "Enabling fast charging—vehicle considerations." *J. Power Sources*, **367**, 216 (2017).
17. A. Burnham et al., "Enabling fast charging—infrastructure and economic considerations." *J. Power Sources*, **367**, 237 (2017).
18. X. G. Yang, T. Liu, Y. Gao, S. Ge, Y. Leng, D. Wang, and C. Y. Wang, "Asymmetric temperature modulation for extreme fast charging of lithium-ion batteries." *Joule*, **3**, 3002 (2019).
19. P. M. Attia et al., "Closed-loop optimization of fast-charging protocols for batteries with machine learning." *Nature*, **578**, 397 (2020).
20. H. Zheng, G. Liu, X. Song, P. Ridgway, S. Xun, and V. S. Battaglia, "Cathode performance as a function of inactive material and void fractions." *J. Electrochem. Soc.*, **157**, A1060 (2010).
21. S.-L. Wu, W. Zhang, X. Song, A. K. Shukla, G. Liu, V. Battaglia, and V. Srinivasan, "High rate capability of Li(Ni 1/3 Mn 1/3 Co 1/3)O 2 electrode for li-ion batteries." *J. Electrochem. Soc.*, **159**, A438 (2012).
22. H. Zheng, R. Yang, G. Liu, X. Song, and V. S. Battaglia, "Cooperation between active material, polymeric binder and conductive carbon additive in lithium ion battery cathode." *J. Phys. Chem. C*, **116**, 4875 (2012).
23. H. Zheng, Q. Qu, G. Zhu, G. Liu, V. S. Battaglia, and H. Zheng, "Quantitative characterization of the surface evolution for LiNi0.5Co0.2Mn0.3O2/graphite cell during long-term cycling." *ACS Appl. Mater. Interfaces*, **9**, 12445 (2017).
24. H. E. L. Batteries et al., "Advanced materials processing and novel characterization methods for low- cost, Higher energy-density lithium-ion batteries." *Advanced Automotive Battery Conference* (2013).
25. C. J. Bae, C. K. Erdonmez, J. W. Halloran, and Y. M. Chiang, "Design of battery electrodes with dual-scale porosity to minimize tortuosity and maximize performance." *Adv. Mater.*, **25**, 1254 (2013).
26. K. Xu, "Nonaqueous liquid electrolytes for lithium-based rechargeable batteries." *Chem. Rev.*, **104**, 4303 (2004).
27. K. Xu, "Electrolytes and interphases in li-ion batteries and beyond." *Chem. Rev.*, **114**, 11503 (2014).
28. L. Suo, O. Borodin, T. Gao, M. Olguin, J. Ho, X. Fan, C. Luo, C. Wang, and K. Xu, "'Water-in-salt' electrolyte enables high-voltage aqueous lithium-ion chemistries." *Science (80-.).*, **350**, 938 (2015).
29. S. S. Zhang, K. Xu, and T. R. Jow, "A new approach toward improved low temperature performance of li-ion battery." *Electrochem. Commun.*, **4**, 928 (2002).
30. C. Y. Wang, G. Zhang, S. Ge, T. Xu, Y. Ji, X. G. Yang, and Y. Leng, "Lithium-ion battery structure that self-heats at low temperatures." *Nature*, **529**, 515 (2016).
31. X. G. Yang, G. Zhang, S. Ge, and C. Y. Wang, "Fast charging of lithium-ion batteries at all temperatures." *Proc. Natl. Acad. Sci. U. S. A* (2018)**115**(28), 7266.
32. A. Mistry, A. Verma, and P. P. Mukherjee, "Controllable electrode stochasticity self-heats lithium-ion batteries at low temperatures." *ACS Appl. Mater. Interfaces*, **11**, 26764 (2019).
33. Y. Liu, Y. Zhu, and Y. Cui, "Challenges and opportunities towards fast-charging battery materials." *Nat. Energy*, **4**, 540 (2019).
34. J. Sieg, J. Bandlow, T. Mitsch, D. Dragicevic, T. Materna, B. Spier, H. Witzenhausen, M. Ecker, and D. U. Sauer, "Fast charging of an electric vehicle lithium-ion battery at the limit of the lithium deposition process." *J. Power Sources*, **427**, 260 (2019).

35. T. R. Tanim et al., "Extreme fast charge challenges for lithium-ion battery: variability and positive electrode issues." *J. Electrochem. Soc.*, **166**, A1926 (2019).
36. A. N. Mistry, K. Smith, and P. P. Mukherjee, "Secondary-phase stochastics in lithium-ion battery electrodes." *ACS Appl. Mater. Interfaces*, **10**, 6317 (2018).
37. A. Mistry, *Mesoscale Interactions in Porous Electrodes.*, Purdue University (2019), DOI: https://doi.org/10.25394/PGS.8038682.v1.
38. F. L. E. Usseglio-Viretta et al., "Resolving the discrepancy in tortuosity factor estimation for li-ion battery electrodes through micro-macro modeling and experiment." *J. Electrochem. Soc.*, **165**, A3403 (2018).
39. D. Lasseux and F. J. Valdes-Parada, "Symmetry properties of macroscopic transport coefficients in porous media." *Phys. Fluids*, **29**, 43303 (2017).
40. O. Rozenbaum and S. R. Du Roscoat, "Representative elementary volume assessment of three-dimensional X-ray microtomography images of heterogeneous materials: application to limestones." *Phys. Rev. E - Stat. Nonlinear, Soft Matter Phys.*, **89**, 53304 (2014).
41. J. Newman and W. Tiedemann, "Porous-electrode theory with battery applications." *AIChE J.*, **21**, 25 (1975).
42. M. Doyle, T. F. Fuller, and J. Newman, "Modeling of galvanostatic charge and discharge of the lithium/polymer/insertion cell." *J. Electrochem. Soc.*, **140**, 1526 (1993).
43. B. L. Trembacki, D. R. Noble, M. E. Ferraro, and S. A. Roberts, "Mesoscale effects of composition and calendering in lithium-ion battery composite electrodes." *J. Electrochem. Energy Convers. Storage*, **17**, 041001 (2020).
44. R. B. Bird, W. E. Stewart, and E. N. Lightfoot, *Transport Phenomena* (John Wiley & Sons, New York) (2002).
45. A. N. Mistry, K. Smith, and P. P. Mukherjee, "Electrochemistry coupled mesoscale complexations in electrodes lead to thermo-electrochemical extremes." *ACS Appl. Mater. Interfaces*, **10**, 28644 (2018).
46. A. N. Mistry and P. P. Mukherjee, "Probing spatial coupling of resistive modes in porous intercalation electrodes through impedance spectroscopy." *Phys. Chem. Chem. Phys.*, **21**, 3805 (2019).
47. A. Mistry, D. Juarez-Robles, M. Stein, K. Smith, and P. P. Mukherjee, "Analysis of long-range interaction in lithium-ion battery electrodes." *J. Electrochem. Energy Convers. Storage*, **13**, 031006 (2016).
48. M. M. Forouzan, B. A. Mazzeo, and D. R. Wheeler, "Modeling the effects of electrode microstructural heterogeneities on li-ion battery performance and lifetime." *J. Electrochem. Soc.*, **165**, A2127 (2018).
49. S. Müller, J. Eller, M. Ebner, C. Burns, J. Dahn, and V. Wood, "Quantifying inhomogeneity of lithium ion battery electrodes and its influence on electrochemical performance." *J. Electrochem. Soc.*, **165**, A339 (2018).
50. A. W. Abboud, E. J. Dufek, and B. Liaw, "Communication—implications of local current density variations on lithium plating affected by cathode particle size." *J. Electrochem. Soc.*, **166**, A667 (2019).
51. Y. Yang et al., "Quantification of heterogeneous degradation in li-ion batteries." *Adv. Energy Mater.*, **9**, 1900674 (2019).
52. D. Kehrwald, P. R. Shearing, N. P. Brandon, P. K. Sinha, and S. J. Harris, "Local tortuosity inhomogeneities in a lithium battery composite electrode." *J. Electrochem. Soc.*, **158**, A1393 (2011).
53. S. J. Harris and P. Lu, "Effects of inhomogeneities–nanoscale to mesoscale–on the durability of li-ion batteries." *J. Phys. Chem. C*, **117**, 6481 (2013).
54. K. Smith, F. L. E. Usseglio-Viretta, A. M. Colclasure, W. Mai, A. N. Mistry, P. P. Mukherjee, S. Santhanagopalan, and M. Keyser, "Modeling of lithium plating induced by heterogeneities at varied length-scales in lithium-ion batteries." *Meeting Abstracts; The Electrochemical Society*, p. 1136 (2019).
55. M. E. Ferraro, B. L. Trembacki, V. E. Brunini, D. R. Noble, and S. A. Roberts, "Electrode mesoscale as a collection of particles: coupled electrochemical and mechanical analysis of NMC cathodes." *J. Electrochem. Soc.*, **167**, 013543 (2020).
56. S. Hein et al., "Influence of conductive additives and binder on the impedance of lithium-ion battery electrodes: effect of morphology." *J. Electrochem. Soc.*, **167**, 013546 (2020).
57. A. Shodiev, E. N. Primo, M. Chouchane, T. Lombardo, A. C. Ngandjong, A. Rucci, and A. A. Franco, "4D-resolved physical model for electrochemical impedance spectroscopy of li(Ni1-x-YMnxCoy)O2-based cathodes in symmetric cells: consequences in tortuosity calculations." *J. Power Sources*, **454**, 227871 (2020).
58. A. Mistry, K. Smith, and P. P. Mukherjee, "Stochasticity at scales leads to lithium intercalation cascade." *ACS Appl. Mater. Interfaces*, **12**, 16359 (2020).
59. P. Liu, R. Xu, Y. Liu, F. Lin, and K. Zhao, "Computational modeling of heterogeneity of stress, charge, and cyclic damage in composite electrodes of Li-Ion batteries." *J. Electrochem. Soc.*, **167**, 040527 (2020).
60. A. C. Ngandjong, A. Rucci, M. Maiza, G. Shukla, J. Vazquez-Arenas, and A. A. Franco, "Multiscale simulation platform linking lithium ion battery electrode fabrication process with performance at the cell level." *J. Phys. Chem. Lett.*, **8**, 5966 (2017).
61. Stephen J. Harris and Peng Lu, "Effects of inhomogeneities—nanoscale to mesoscale—on the durability of Li-Ion." *J. Phys. Chem. C*, **117**, 6481 (2013).
62. N. Ghanbari, T. Waldmann, M. Kasper, P. Axmann, and M. Wohlfahrt-Mehrens, "Inhomogeneous degradation of graphite anodes in li-ion cells: a postmortem study using glow discharge optical emission spectroscopy (GD-OES)." *J. Phys. Chem. C*, **120**, 22225 (2016).
63. K. P. C. Yao, J. S. Okasinski, K. Kalaga, I. A. Shkrob, and D. P. Abraham, "Quantifying lithium concentration gradients in the graphite electrode of Li-Ion cells using: operando energy dispersive X-ray diffraction." *Energy Environ. Sci.*, **12**, 656 (2019).
64. D. P. Finegan et al., "Spatially resolving lithiation in silicon-graphite composite electrodes via in situ high-energy X-ray diffraction computed tomography." *Nano Lett.*, **19**, 3811 (2019).
65. Y. Zhang, F. Yan, J. Ma, M. Yan, M. Ni, and C. Xia, "In operando monitoring of reaction-diffusion streamlines and uncovering of electrochemo-structural interactions in electrodes." *J. Mater. Chem. A*, **7**, 10256 (2019).
66. M. Wetjen, M. Trunk, L. Werner, H. A. Gasteiger, R. Gernhäuser, R. Gilles, B. Märkisch, and Z. Révay, "Monitoring the lithium concentration across the thickness of silicon-graphite electrodes during the first (De-)lithiation." *J. Electrochem. Soc.*, **166**, A1408 (2019).
67. H. Liu, S. Kazemiabnavi, A. Grenier, G. Vaughan, M. Di Michiel, B. J. Polzin, K. Thornton, K. W. Chapman, and P. J. Chupas, "Quantifying reaction and rate heterogeneity in battery electrodes in 3D through operando X-ray diffraction computed tomography." *ACS Appl. Mater. Interfaces*, **11**, 18386 (2019).
68. J. M. Paz-Garcia, O. O. Taiwo, E. Tudisco, D. P. Finegan, P. R. Shearing, D. J. L. Brett, and S. A. Hall, "4D analysis of the microstructural evolution of si-based electrodes during lithiation: time-lapse X-ray imaging and digital volume correlation." *J. Power Sources*, **320**, 196 (2016).
69. M. Ebner, F. Marone, M. Stampanoni, and V. Wood, "Visualization and quantification of electrochemical and mechanical degradation in li ion batteries." *Science (80-.).*, **342**, 716 (2013).
70. M. J. Mühlbauer, A. Schökel, M. Etter, V. Baran, and A. Senyshyn, "Probing chemical heterogeneity of li-ion batteries by in operando high energy X-ray diffraction radiography." *J. Power Sources*, **403**, 49 (2018).
71. E. P. Jahrman, L. A. Pellerin, A. S. Ditter, L. R. Bradshaw, T. T. Fister, B. J. Polzin, S. E. Trask, A. R. Dunlop, and G. T. Seidler, "Laboratory-Based X-ray Absorption spectroscopy on a working pouch cell battery at industrially-relevant charging rates." *J. Electrochem. Soc.*, **166**, A2549 (2019).
72. P. Pietsch and V. Wood, "X-Ray tomography for lithium ion battery research: a practical guide." *Annu. Rev. Mater. Res.*, **47**, 451 (2017).
73. T. M. M. Heenan, C. Tan, J. Hack, D. J. L. Brett, and P. R. Shearing, "Developments in X-ray tomography characterization for electrochemical devices." *Mater. Today*, **31**, 69 (2019).
74. A. Mistry, "The 2018 Edward G. Weston summer research fellowship—summary report: curvature effects in precipitation dynamics." *Electrochem. Soc. Interface*, **27**, 80 (2018).
75. B. L. Trembacki, A. N. Mistry, D. R. Noble, M. E. Ferraro, P. P. Mukherjee, and S. A. Roberts, "Editors' choice—mesoscale analysis of conductive binder domain morphology in lithium-ion battery electrodes." *J. Electrochem. Soc.*, **165**, E725 (2018).
76. B. L. Trembacki, D. R. Noble, V. E. Brunini, M. E. Ferraro, and S. A. Roberts, "Mesoscale effective property simulations incorporating conductive binder." *J. Electrochem. Soc.*, **164**, E3613 (2017).
77. M. Chouchane, A. Rucci, T. Lombardo, A. C. Ngandjong, and A. A. Franco, "Lithium ion battery electrodes predicted from manufacturing simulations: assessing the impact of the carbon-binder spatial location on the electrochemical performance." *J. Power Sources*, **444**, 227285 (2019).
78. A. Mistry and P. P. Mukherjee, "Deconstructing electrode pore network to learn transport distortion." *Phys. Fluids*, **31**, 122005 (2019).
79. T. Rajendra, A. N. Mistry, P. Patel, L. J. Ausderau, X. Xiao, P. P. Mukherjee, and G. J. Nelson, "Quantifying transport, geometrical, and morphological parameters in li-ion cathode phases using X-ray microtomography." *ACS Appl. Mater. Interfaces*, **11**, 19933 (2019).
80. G. Liu, H. Zheng, S. Kim, Y. Deng, A. M. Minor, X. Song, and V. S. Battaglia, "Effects of various conductive additive and polymeric binder contents on the performance of a lithium-ion composite cathode." *J. Electrochem. Soc.*, **155**, A887 (2008).
81. H. Zheng, L. Tan, G. Liu, X. Song, and V. S. Battaglia, "Calendering effects on the physical and electrochemical properties of Li[Ni 1/3Mn 1/3Co 1/3]O 2 Cathode." *J. Power Sources*, **208**, 52 (2012).
82. G. Liu, H. Zheng, X. Song, and V. S. Battaglia, "Particles and polymer binder interaction: a controlling factor in lithium-ion electrode performance." *J. Electrochem. Soc.*, **159**, A214 (2012).
83. M. Stein, A. Mistry, and P. P. Mukherjee, "Mechanistic understanding of the role of evaporation in electrode processing." *J. Electrochem. Soc.*, **164**, A1616 (2017).
84. P. P. Mukherjee and A. N. Mistry, "Hierarchy of stochastic scales in intercalation electrodes." *Meeting Abstracts; The Electrochemical Society*, p. 1135 (2019).
85. W. Mai, F. L. E. Usseglio-Viretta, A. M. Colclasure, and K. Smith, "Enabling fast charging of lithium-ion batteries through secondary-/dual- pore network: part II—numerical model." *Electrochim. Acta*, **341**, 136013 (2020).
86. A. M. Colclasure et al., "Electrode scale and electrolyte transport effects on extreme fast charging of lithium-ion cells." *Electrochim. Acta*, **337**, 135854 (2020).
87. S. Jaiser, J. Kumberg, J. Klaver, J. L. Urai, W. Schabel, J. Schmatz, and P. Scharfer, "Microstructure formation of lithium-ion battery electrodes during drying—an ex-situ study using cryogenic broad ion beam slope-cutting and scanning electron microscopy (Cryo-BIB-SEM)." *J. Power Sources*, **345**, 97 (2017).
88. M. Ebner, D. W. Chung, R. E. García, and V. Wood, "Tortuosity anisotropy in lithium-ion battery electrodes." *Adv. Energy Mater.*, **4**, 1301278 (2014).
89. J. Newman and K. E. Thomas-Alyea, *Electrochemical Systems* (John Wiley & Sons, New York) (2012).
90. M. Park, X. Zhang, M. Chung, G. B. Less, and A. M. Sastry, "A review of conduction phenomena in li-ion batteries." *J. Power Sources*, **195**, 7904 (2010).

91. R. D. Minter, D. Juarez-Robles, C. Fear, Y. Barsukov, and P. P. Mukherjee, "Three-electrode coin cell preparation and electrodeposition analytics for lithium-ion batteries." *J. Vis. Exp.*, **2018**, e57735. (2018).
92. M.-T. F. Rodrigues, K. Kalaga, S. E. Trask, D. W. Dees, I. A. Shkrob, and D. P. Abraham, "Fast charging of li-ion cells: part I. Using li/cu reference electrodes to probe individual electrode potentials." *J. Electrochem. Soc.*, **166**, A996 (2019).
93. X. G. Yang, S. Ge, T. Liu, Y. Leng, and C. Y. Wang, "A look into the voltage plateau signal for detection and quantification of lithium plating in lithium-ion cells." *J. Power Sources*, **395**, 251 (2018).
94. P. Arora, "Mathematical modeling of the lithium deposition overcharge reaction in lithium-ion batteries using carbon-based negative electrodes." *J. Electrochem. Soc.*, **146**, 3543 (1999).
95. D. Ren, K. Smith, D. Guo, X. Han, X. Feng, L. Lu, M. Ouyang, and J. Li, "Investigation of lithium plating-stripping process in li-ion batteries at low temperature using an electrochemical model." *J. Electrochem. Soc.*, **165**, A2167 (2018).
96. C. von Lüders, J. Keil, M. Webersberger, and A. Jossen, "Modeling of lithium plating and lithium stripping in lithium-ion batteries." *J. Power Sources*, **414**, 41 (2019).
97. T. Waldmann, M. Kasper, and M. Wohlfahrt-Mehrens, "Optimization of charging strategy by prevention of lithium deposition on anodes in high-energy lithium-ion batteries - electrochemical experiments." *Electrochim. Acta*, **178**, 525 (2015).
98. T. Waldmann, B.-I. Hogg, M. Kasper, S. Grolleau, C. G. Couceiro, K. Trad, B. P. Matadi, and M. Wohlfahrt-Mehrens, "Interplay of operational parameters on lithium deposition in lithium-ion cells: systematic measurements with reconstructed 3-electrode pouch full cells." *J. Electrochem. Soc.*, **163**, A1232 (2016).
99. T. Waldmann, B. I. Hogg, and M. Wohlfahrt-Mehrens, "Li plating as unwanted side reaction in commercial li-ion cells—a review." *J. Power Sources*, **384**, 107 (2018).
100. J. Landesfeind, J. Hattendorff, A. Ehrl, W. A. Wall, and H. A. Gasteiger, "Tortuosity determination of battery electrodes and separators by impedance spectroscopy." *J. Electrochem. Soc.*, **163**, A1373 (2016).
101. A. N. Mistry, H. R. Palle, and P. P. Mukherjee, "In operando thermal signature probe for lithium-ion batteries." *Appl. Phys. Lett.*, **114**, 023901 (2019).
102. A. Mistry, S. Rangaranjan, and P. P. Mukherjee, "Probing signatures of thermal metastability in lithium-ion batteries." *ECS Meeting Abstracts*, A05 (2019).
103. S. Huang, X. Wu, G. M. Cavalheiro, X. Du, B. Liu, Z. Du, and G. Zhang, "In Situ measurement of lithium-ion cell internal temperatures during extreme fast charging." *J. Electrochem. Soc.*, **166**, A3254 (2019).
104. K. Shah, V. Vishwakarma, and A. Jain, "Measurement of multiscale thermal transport phenomena in li-ion cells: a review." *J. Electrochem. Energy Convers. Storage*, **13**, 30801 (2016).
105. M. B. Ahmed, S. Shaik, and A. Jain, "Measurement of radial thermal conductivity of a cylinder using a time-varying heat flux method." *Int. J. Therm. Sci.*, **129**, 301 (2018).
106. G. Zhang, H. Tian, S. Ge, D. Marple, F. Sun, and C. Y. Wang, "Visualization of self-heating of an all climate battery by infrared thermography." *J. Power Sources*, **376**, 111 (2018).
107. J. B. Robinson, J. A. Darr, D. S. Eastwood, G. Hinds, P. D. Lee, P. R. Shearing, O. O. Taiwo, and D. J. L. Brett, "Non-uniform temperature distribution in li-ion batteries during discharge - a combined thermal imaging, X-ray micro-tomography and electrochemical impedance approach." *J. Power Sources*, **252**, 51 (2014).
108. A. Mistry, C. Fear, R. Carter, C. T. Love, and P. P. Mukherjee, "Electrolyte confinement alters lithium electrodeposition." *ACS Energy Lett.*, **4**, 156 (2019).
109. P. Bai, J. Li, F. R. Brushett, and M. Z. Bazant, "Transition of lithium growth mechanisms in liquid electrolytes." *Energy Environ. Sci.*, **9**, 3221 (2016).
110. G. Bieker, M. Winter, and P. Bieker, "Electrochemical in situ investigations of SEI and dendrite formation on the lithium metal anode." *Phys. Chem. Chem. Phys.*, **17**, 8670 (2015).
111. K. H. Chen, K. N. Wood, E. Kazyak, W. S. Lepage, A. L. Davis, A. J. Sanchez, and N. P. Dasgupta, "Dead lithium: mass transport effects on voltage, capacity, and failure of lithium metal anodes." *J. Mater. Chem. A*, **5**, 11671 (2017).
112. Aashutosh Mistry and Partha P. Mukherjee, "Molar Volume Mismatch: a Malefactor for Irregular Metallic Electrodeposition with Solid Electrolytes." *Journal of the Electrochemical Society*, **167** (2019).
113. A. Mistry and V. Srinivasan, "On Our Limited Understanding of Electrodeposition." *MRS Adv.*, **4**, 2843 (2019).
114. M. Pathak, S. Kolluri, T. Jang, C. Pathak, S. Santhanagopalan, and V. R. Subramanian, "Model-based battery management system of lithium-ion batteries." *Meeting Abstracts; The Electrochemical Society*, p. 1129 (2019).
115. M. Pathak, S. Kolluri, and V. R. Subramanian, "Generic model control for lithium-ion batteries." *J. Electrochem. Soc.*, **164**, A973 (2017).
116. D. Juarez-Robles, C.-F. Chen, Y. Barsukov, and P. Mukherjee, "Impedance evolution characteristics in lithium-ion batteries." *J. Electrochem. Soc.*, **164**, A837 (2017).
117. J. E. Harlow, S. L. Glazier, J. Li, and J. R. Dahn, "Use of asymmetric average charge- and average discharge- voltages as an indicator of the onset of unwanted lithium deposition in lithium-ion cells." *J. Electrochem. Soc.*, **165**, A3595 (2018).
118. B. Delattre, R. Amin, J. Sander, J. De Coninck, A. P. Tomsia, and Y.-M. Chiang, "Impact of pore tortuosity on electrode kinetics in lithium battery electrodes: study in directionally freeze-cast LiNi 0.8 Co 0.15 Al 0.05 O 2 (NCA)." *J. Electrochem. Soc.*, **165**, A388 (2018).
119. S. J. Harris, A. Timmons, D. R. Baker, and C. Monroe, "Direct in situ measurements of li transport in li-ion battery negative electrodes." *Chem. Phys. Lett.*, **485**, 265 (2010).
120. K. E. Thomas-Alyea, C. Jung, R. B. Smith, and M. Z. Bazant, "In situ observation and mathematical modeling of lithium distribution within graphite." *J. Electrochem. Soc.*, **164**, E3063 (2017).
121. S. J. Harris, E. K. Rahani, and V. B. Shenoy, "Direct in situ observation and numerical simulations of non-shrinking-core behavior in an MCMB graphite composite electrode." *J. Electrochem. Soc.*, **159**, A1501 (2012).
122. J. Wandt, P. Jakes, J. Granwehr, R. A. Eichel, and H. A. Gasteiger, "Quantitative and time-resolved detection of lithium plating on graphite anodes in lithium ion batteries." *Mater. Today*, **21**, 231 (2018).
123. D. Halliday, R. Resnick, and J. Walker, *Fundamentals of Physics* (John Wiley & Sons, New York) (2013).
124. A. N. Mistry and P. P. Mukherjee, "Analyzing the importance of particle morphology and heterogeneity in li-ion battery electrodes." *ECS Meeting Abstracts; The Electrochemical Society*A03 (2018).
125. G. J. Nelson, L. J. Ausderau, S. Shin, J. R. Buckley, A. Mistry, P. P. Mukherjee, and V. De Andrade, "Transport-geometry interactions in li-ion cathode materials imaged using X-ray nanotomography." *J. Electrochem. Soc.*, **164**, A1412 (2017).
126. K. G. Gallagher, D. W. Dees, A. N. Jansen, D. P. Abraham, and S.-H. Kang, "A volume averaged approach to the numerical modeling of phase-transition intercalation electrodes presented for Li x C 6." *J. Electrochem. Soc.*, **159**, A2029 (2012).
127. D. R. Baker and M. W. Verbrugge, "Intercalate diffusion in multiphase electrode materials and application to lithiated graphite." *J. Electrochem. Soc.*, **159**, A1341 (2012).
128. N. Kotak, P. Barai, A. Verma, A. Mistry, and P. P. Mukherjee, "Electrochemistry-mechanics coupling in intercalation electrodes." *J. Electrochem. Soc.*, **165**, A1064 (2018).